Title

Conformational Transition Pathway in the Inhibitor Binding Process of Human Monoacylglycerol Lipase

Journal

Protein Journal, 33(6)

ISSN

1572-3887

Authors

Chen, H
Tian, R
Ni, Z
et al.

Publication Date

2014-11-21

DOI

10.1007/s10930-014-9572-z

Peer reviewed

Protein J (2014) 33:503–511
DOI 10.1007/s10930-014-9572-z

Conformational Transition Pathway in the Inhibitor Binding Process of Human Monoacylglycerol Lipase

Huayou Chen · Rui Tian · Zhong Ni · Zhongge Zhang · Hongzhang Chen · Qi Guo · Milton H. Saier Jr.

Published online: 31 July 2014

Abstract Human monoacylglycerol lipase (MGL) catalyzes the hydrolysis of 2-arachidonoylglycerol to arachidonic and glycerol, which plays a pivotal role in the normal biological processes of brain. Co-crystal structure of the MGL in complex with its inhibitor, compound **1**, shows that the helix α4 undergoes large-scale conformational changes in response to the compound **1** binding compared to the *apo* MGL. However, the detailed conformational transition pathway of the helix α4 in the inhibitor binding process of MGL has remained unclear. Here, conventional molecular dynamics (MD) and nudged elastic band (NEB) simulations were performed to explore the conformational transition pathway of the helix α4. Conventional MD simulations unveiled that the compound **1** induced the closed conformation of the active site of MGL, reduced the conformational flexibility of the helix α4, and elicited the large-scale conformational rearrangement of the helix α4, leading to the complete folding of the helix α4. Moreover, NEB simulations revealed that the conformational transition pathway of helix α4 underwent an almost 180° counter-clockwise rotation of the helix α4. Our computational results advance the structural and mechanistic understanding of the inhibitory mechanism.

Keywords MGL · MD simulations · Nudged elastic band · Conformational transition pathway

Abbreviations

2-AG	2-Arachidonoylglycerol
CNS	Central nervous system
DCCM	Dynamical cross-correlation matrices
DSSP	Defined secondary structure of proteins
MD	Molecular dynamics
MGL	Monoacylglycerol lipase
NEB	Nudged elastic band
RMSD	Root-mean-square deviation
RMSF	Root-mean-square fluctuation

1 Introduction

2-Arachidonoylglycerol (2-AG), an endogenous ligand, acts as a potent agonist that activates G-protein-coupled cannabinoid receptors CB_1 and CB_2, which are involved in diverse physiological processes encompassing mood, pain-sensation, and memory [1, 2]. 2-AG is tightly regulated by human monoacylglycerol lipase (MGL; EC 3.1.1.23), an ubiquitous 33 kDa, membrane-associated member of the serine hydrolase superfamily [3–5]. MGL contains the quintessential GXSXG, where X is any amino acid, conserved sequence shared by the vast majority of serine hydrolases. The three residues Ser122, His269, and Asp239 constitute the catalytic reaction center of MGL [3].

Electronic supplementary material The online version of this article (doi:10.1007/s10930-014-9572-z) contains supplementary material, which is available to authorized users.

H. Chen · R. Tian · Z. Ni · Q. Guo
Institute of Life Sciences, Jiangsu University, Zhenjiang 212013, China

H. Chen · Z. Zhang · M. H. Saier Jr. (✉)
Division of Biological Sciences, University of California at San Diego, La Jolla, CA 92093-0116, USA
e-mail: saiermh@gmail.com; msaier@ucsd.edu

H. Chen · H. Chen
National Key Laboratory of Biochemical Engineering, Institute of Process Engineering, Chinese Academy of Sciences, Beijing 10090, China

Scheme 1 MGL catalyzes 2-arachidonoylglycerol to arachidonic and glycerol

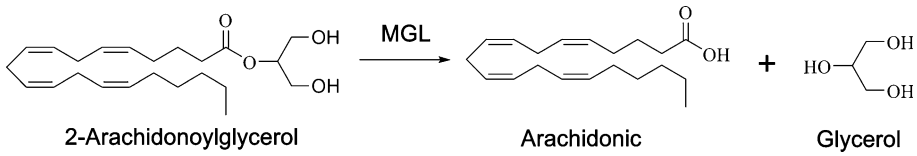

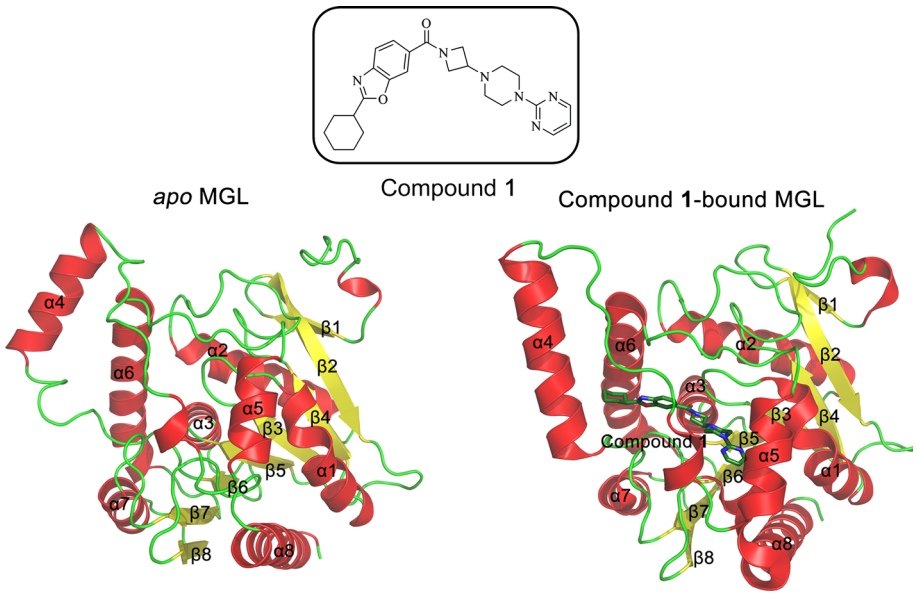

Fig. 1 Cartoon representation of the *apo* (PDB ID: 3HJU) and compound **1**-bound (PDB ID: 3PE6) MGL. The secondary structures of α-helices, β-sheets and loops are colored by *red*, *yellow* and *green*. The compound **1** (stick representation) occupies the active site of MGL surrounded by loops connecting helices α4–α6. *Inset*: Structure of compound **1** (Color figure online)

The functional roles of MGL are tissue specific. In adipose tissue, MGL appears to follow the action of hormone-sensitive lipase to completely catalyze intracellular triglyceride to fatty acids and glycerol [6]. In the central nervous system (CNS), MGL hydrolyzes 2-AG to arachidonic and glycerol, which plays an essential role in the regulation of endocannabinoid signaling (Scheme 1) [7]. An overexpression of MGL in the CNS has been associated with various neurological diseases because immoderate hydrolysis of 2-AG impairs the physiological roles of CB_1 and CB_2 [8, 9]. These findings have motivated the development of MGL inhibitors, including a non-covalent inhibitor URB602 with low potency and selectivity for MGL [10] and irreversible covalent inhibitors such as 4-nitrophenyl-carbamate JZL184 [11], *N*-arachidonylmaleimide [12], and SAR629 [13].

Recently, Schalk-Hihi et al. [14] reported a high-resolution structure of a soluble form of human MGL in complex with its reversible inhibitor, compound **1**. This new co-crystal structure unveils a unique conformation of the regulatory lid-domain of MGL. By comparison of inhibitor-bound and unbound structures illustrates that the compound **1** induces a closed conformation of the regulatory important lid-domain. More specially, the helix α4 (residues 153–170) of the lid-domain undergoes a significant conformational change from the uncoiling state of the N-terminal residues (residues 153–157) in the *apo* MGL to the complete folding of the helix α4 in the compound **1**-bound MGL (Fig. 1). However, the detailed conformational transition pathway of the helix α4 in the inhibitor binding process has remained unclear.

Here, computational studies that integrate conventional molecular dynamics (MD) and nudged elastic band (NEB) simulations were conducted to explore the conformational transition pathway of the helix α4 in the inhibitor binding process of human MGL. The obtained results are not only of fundamental importance to understand the inhibitory mechanism of MGL, but also to design potent and selective MGL inhibitors.

2 Materials and Methods

2.1 Simulation Systems

Initial coordinates for the *apo* and compound **1**-bound states of human MGL were taken from X-ray crystal structures (Protein Data Bank ID 3HJU [15] and 3PE6 [14], respectively). In the inhibitor complex structure [14], the three introduced mutations, K36A, L169S, and L176S, were mutated to native residues. Partial atomic charges for the compound **1** were calculated using the restricted electrostatic potential fitting protocol implemented in the Antechamber module of the AMBER 11 program [16] and following electrostatic potential calculations at ab initio HF/6-31G* level using Gaussian 09 program [17]. The

protein was modeled using the AMBER FF03 force field [18]. For the simulations of MGL in aqueous solution, a truncated octahedral box of TIP3P waters [19] was added with a 10 Å buffer around the protein. The appropriate number of counter-ions was added to maintain the electroneutrality of the two systems.

2.2 Conventional MD Simulation

Energy minimizations, including steepest descent and conjugate gradient algorithms, were carried out to remove bad contacts in the initial structures using the previously reported protocol [20–22]. After relaxation, the two systems were heated from 0 to 300 K in 200 ps, which was followed by constant temperature equilibration at 300 K for 300 ps. Finally, 100 ns MD simulations were carried out for each system in an isothermal isobaric ensemble (NPT) with periodic boundary conditions. An integration step of 2 fs was set for the MD simulations, and the long-range electrostatic interactions were treated by the particle mesh Ewald (PME) method [23]. 10 Å was used for long range electrostatics and van der Waals interactions. The SHAKE method [24] was applied to constrain all covalent bonds involving hydrogen atoms. Each simulation was coupled to a 300 K thermal bath at 1.0 atm using the Langevin algorithm [25].

2.3 Dynamical Cross-Correlation Matrices (DCCM)

The C_α dynamical DCCM was calculated to uncover correlative motions of protein domains [26]. $C(i,j)$ was computed be means of Eq. (1):

$$C(i,j) = \frac{c(i,j)}{c(i,i)^{1/2}c(j,j)^{1/2}} \tag{1}$$

where $C(i,j)$ is the covariance matrix element of the protein fluctuation between residues i and j.

The value of $C(i,j)$ is calculated from -1 to 1. Positive values indicate positively correlated movement (the same direction), while negative values indicate anti-correlated movement (the opposite direction).

2.4 NEB Simulation

The NEB method [27, 28] was used to investigate the conformational transition pathway for the transformation between the *apo* and compound **1**-bound MGL. In the NEB method, the transition pathway for a conformational change is connected by a string of replicas (or 'images') of the system. Minimization of the entire system, but with the start and the end point structures fixed, provides a minimum energy path. The forces F on each image i in NEB framework are projected to a perpendicular force and a parallel force using a tangent vector (τ) along the path [Eq. (2)]. The perpendicular component of the force is obtained by subtracting out the parallel component of the force [Eq. (3)], where $\nabla V(P_i)$ is the gradient of the energy with respect to the atomic coordinates in the system at image i. The parallel component of the force accounts for the artificial springs linking each image together [Eq. (4)], where k_i is equal to the spring constant between images P_i and P_{i-1}, and P is the 3 N dimensional position vector of image i.

$$F_i = F_i^{\parallel} + F_i^{\perp} \tag{2}$$

$$F_i^{\perp} = -\nabla V(P_i) + ((\nabla V(P_i)) \cdot \boldsymbol{\tau})\tau \tag{3}$$

$$F_i^{\perp} = [(k_{i+1}(P_{i+1} - P_i)) - k_i(P_i - P_{i-1}) \cdot \boldsymbol{\tau}]\tau \tag{4}$$

In the NEB simulation implemented in AMBER 11, the start and end points were taken from the energy-minimized structures of the *apo* and compound **1**-bound MGL from the conventional MD simulations. The initial NEB pathway was composed of eleven staring points followed by eleven end points. The initial path was heated from 0 to 300 K in 300 ps with spring force of 10 kcal mol^{-1} Å^{-2} and Langevin dynamics collision frequency of 1,000 ps^{-1}. Subsequently, the path was equilibrated at 300 K in 500 ps with spring force of 50 kcal mol^{-1} Å^{-2}. After that, 1,010 ps of simulated annealing protocol to calculate minimal energy path with NEB (Table S1) contained quickly heating the path to 500 K, followed by slow cooling to 0 K with the spring force of 50 kcal mol^{-1} Å^{-2}. Finally, 1,000 ps of quenched MD at 0 K were performed to remove any remaining kinetic energy from the path.

3 Results

The crystal architecture of human MGL presents a conserved folding motif named the α/β-hydrolase fold, which is characterized by eight β-sheets including seven parallel strands and one antiparallel strand encased by eight α-helices (Fig. 1). The lid-domain of MGL consists of residues 151–225 from helices α4–α6, which controls substrates access to the active site. The inhibitor, compound **1**, occupies an extended binding site, proximal to helices α4, α6, α7, and α5. The structural characteristics of the *apo* and compound **1**-bound MGL were first probed using conventional MD simulations.

3.1 Protein Stability and Residue Flexibility

Conventional MD simulations of the two systems, *apo* MGL and MGL-compound-**1**, were first performed for

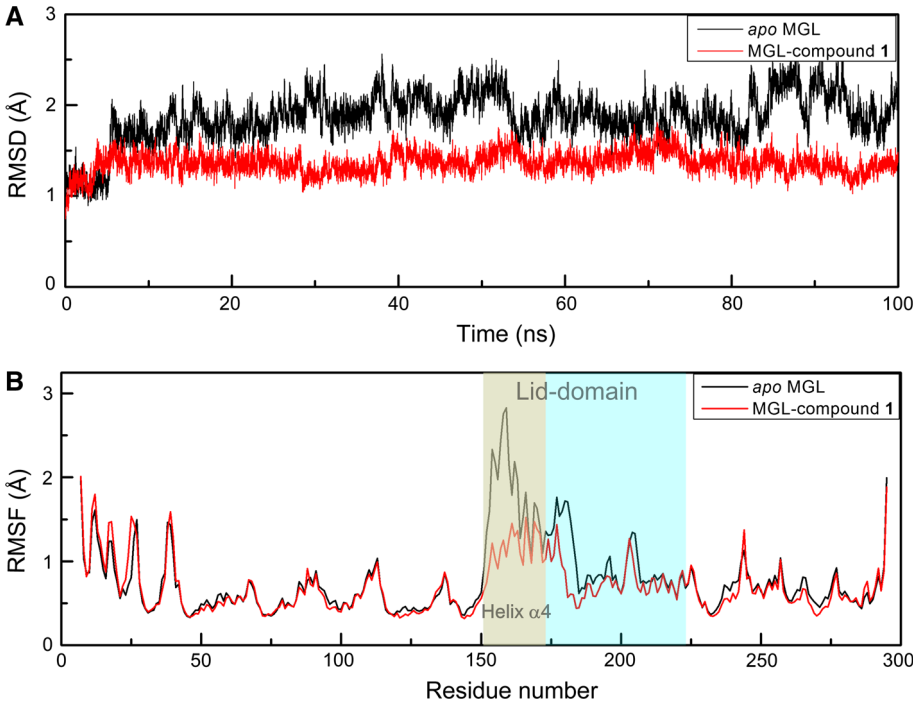

Fig. 2 **a** The RMSD for the C_α atoms of the *apo* and compound **1**-bound MGL during the 100 ns MD simulations. **b** The calculated RMSF values for the C_α atoms of the *apo* and compound **1**-bound MGL

100 ns. The C_α atoms of proteins of the root-mean-square deviation (RMSD) compared to the initial structure was assessed. As shown in Fig. 2a, the C_α atoms RMSD plot for the *apo* MGL seemed to equilibrate at ~5 ns, with the RMSD value of 1.9 ± 0.3 Å. In a similar vein, the C_α atoms RMSD plot for the MGL-compound-**1** complex also tended to equilibrate at ~5 ns, with the RMSD value of 1.4 ± 0.1 Å. These data indicate that the *apo* MGL exhibits a larger conformational flexibility compared with the MGL-compound-**1** complex.

The thermodynamic stability of the two simulated systems can be characterized by their root-mean-square fluctuation (RMSF) values be virtue of the calculation of the C_α atoms fluctuations of each residue around its average position. As shown in Fig. 2b, the residues fluctuations in the *apo* MGL are generally similar with the MGL-compound-**1** complex with the exception of the region in the lid-domain (helix α4 and the loop connecting to α5; residues 153–187 with which the inhibitor interacts), which displays markedly higher RMSF values in the *apo* MGL compared to the MGL-compound-**1** complex.

3.2 Ligand-Induced Closed Conformation of MGL

The superimpositions of the average structures of the *apo* and compound **1**-bound MGL revealed that the compound **1** induced a closed conformation of the active site of MGL, whereas the open conformation was presented in the *apo* MGL (Fig. 3a). To ascertain this distinct dynamic behavior, the C_α atoms distance between Phe159 from the helix α4 and Gly210 from the helix α6 was monitored during MD simulations. As shown in Fig. 3b, the Phe159···Gly210 distance was calculated to be 14.7 ± 0.7 Å in the *apo* MGL, indicative of the open conformation of the active site of MGL. In contrast, this distance was calculated to be 7.8 ± 0.3 Å in the compound **1**-bound MGL, indicative of the closed conformation of the active site of MGL. In the quest of further elucidating the ligand binding on the conformational dynamics of MGL, the influence of correlative motions due to the binding of compound **1** to MGL were evaluated. As shown in Fig. 3c, the results of DCCM indicated that the overall dynamics of the *apo* and compound **1**-bound MGL were very similar to each other. However, inspection of DCCM results between the *apo* and compound **1**-bound MGL unearthed that the compound **1** exerted a significant effect on the conformational dynamics of MGL in several regions; in the *apo* MGL, the helices α4 and α6 that encase the active site of MGL had strong anti-correlated movements, representing by dark blue, whereas in the compound **1**-bound MGL, the anti-correlated movements of the C-lobes significantly reduced after ligand binding. Taken together, these data indicated that the conformational plasticity of the helix α4 was attenuated after the ligand binding.

3.3 Ligand-Induced Complete Folding of Helix α4

Another pronounced structural difference between the average structures of the *apo* and compound **1**-bound MGL emphasized that the helix α4 (residues 158–170), coupled

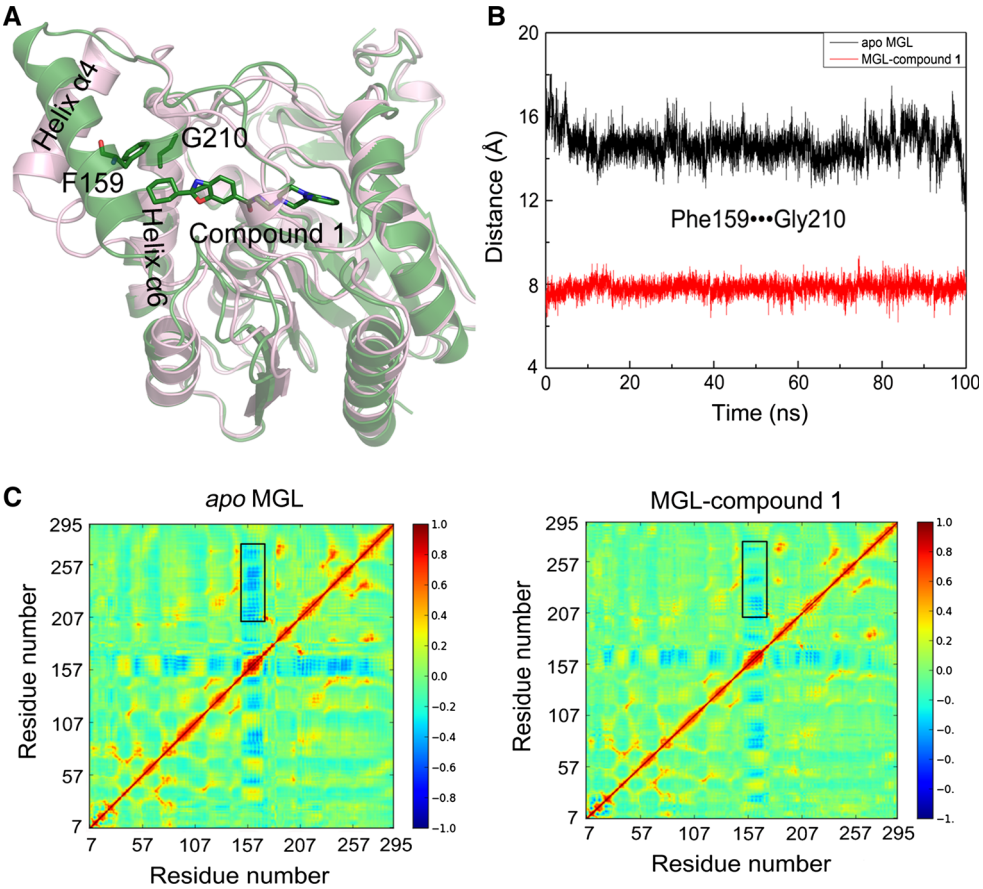

Fig. 3 **a** Overlapping the average structures between the *apo* (*light pink*) and compound **1**-bound (*dark green*) MGL obtained from the MD simulations. **b** The C_α atoms distance between Phe159 and Gly210 for the two simulated systems. **c** The analysis of DCCM for the two simulated systems (Color figure online)

with the uncoiling residues 153–157 at its N-terminus in the *apo* MGL completely integrated into the new helix α4 (residues 153–170) in the compound **1** bound MGL (Fig. 3a). To further address this phenomenon, secondary structure analysis was carried out on residues Pro153 to Val170 for the two simulated systems by the defined secondary structure of proteins (DSSP) algorithm [29]. Figure 4 shows the secondary structure profiles of residues Pro153 to Val170. The native turn secondary structure at residues Pro153 to Thr157 in the *apo* MGL was converted into an α-helical structure in the compound **1**-bound MGL, leading to a complete folding of the helix α4 (residues 153–169) in the ligand bound MGL. In α-helices, a regular pattern of hydrogen bonds exists between an amide carbonyl of residue i (the acceptor) and the amide H^+ donor of residue $i + 4$ ($C_i = O\cdots H\text{–}N_{i+4}$). The hydrogen bond contacts were characterized by percentage of occurrence data [30–32]. The analysis indicated that the $C_i = O^{Pro153}\cdots H\text{–}N_{i+4}^{Thr157}$ was maintained with 100 % occurrence in the compound **1**-bound MGL during the MD simulations, whereas in the *apo* MGL the occurrence of this hydrogen bond was 0 %, in accordance with the results of DSSP. In addition, the angle among the C_α atoms of Pro153, Thr157, and Val161 that orient the same direction located in the helix α4 of the compound **1**-bound MGL was monitored in the two systems during the MD simulations. As shown in Fig. 5, the calculated angle was 125.2° ± 7.5° in the *apo* MGL, revealing the bending of the helix α4. In contrast, it was nearly linear in the compound **1**-bound MGL, with the value of 173.1° ± 4.1°, revealing the complete folding of the helix α4 induced by the compound **1**.

3.4 The Conformational Transition Pathway of Helix α4

Figure 6 shows the angle landscape among the C_α atoms of Pro153, Thr157, and Val161 located in the helix α4 along the transition pathway based on the twenty-two images stemmed from the NEB trajectory. Inspection of the representative snapshots, the process for the conformational transition pathway of helix α4 can be described by the following four states. Figure 6A represents the initial state of helix α4, in which the N-terminal helix α4 (residues 153–157) exhibited the turn secondary structure. In this state, the helix α4 was bending, with the angle ($C_\alpha^{Pro153}\cdots C_\alpha^{Thr157}\cdots C_\alpha^{Val161}$) of 124.3°. Then, the C-terminal helix α4 (residues 158–170) was counter-clockwise rotation (viewed from C to N-terminus), leading to a local maximum of the bending angle of helix α4, with the value of

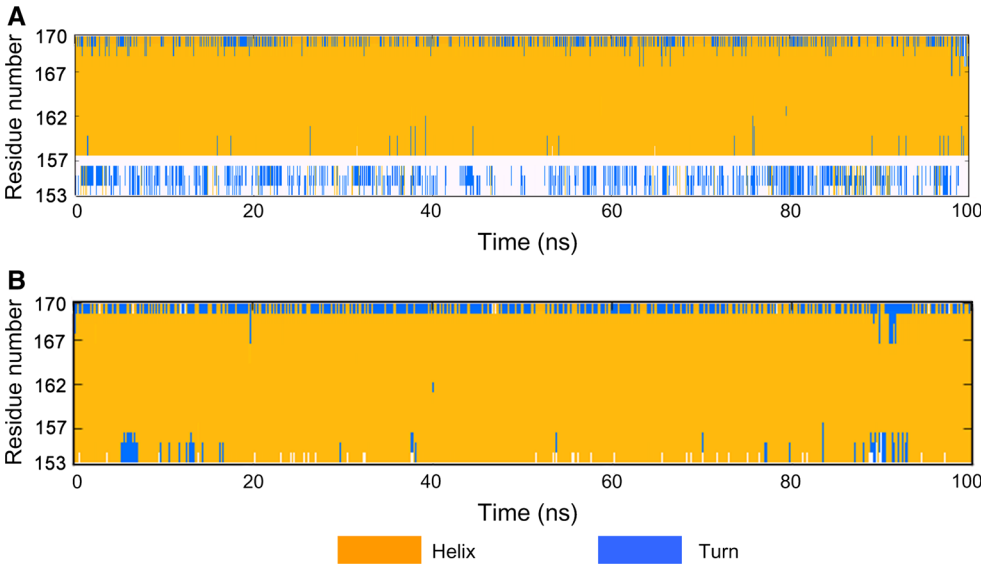

Fig. 4 The analysis of secondary structures for residues 153 to 170 in the *apo* (**a**) and compound **1**-bound (**b**) MGL

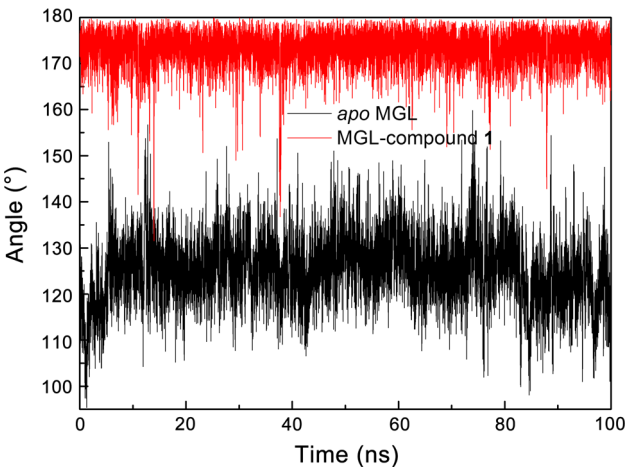

Fig. 5 The calculated angle (C_{α}^{Pro153}···C_{α}^{Thr157}···C_{α}^{Val161}) for the *apo* and compound **1**-bound MGL during the 100 ns MD simulations

150.1° (Fig. 6B). After that, the C-terminal helix α4 was continued to counter-clockwise rotation, coupled with the uncoiling of its several helical residues (residues 158–161) at the start of the C-terminus, giving rise to a local minimum of the bending angle of helix α4, with the value of 129.9° (Fig. 6C). Eventually, the N-terminal residues (153–160) of helix α4 were counter-clockwise rotated to completely fold into an α-helix, which results the maximum angle of 172.9° corresponding to the product structure (Fig. 6D).

4 Discussion

Human MGL has been implicated in the regulation of several cellular events. Inhibition of the aberrant MGL function by inhibitors is emerging as a potential strategy that can be applied to a number of diseases. However, the mechanism of conformational transition pathway for the helix α4 of human MGL in the inhibitor binding process remains unclear. In this article, conventional MD and NEB simulations were carried out to investigate the crystal structure complex of human MGL along with its inhibitor compound **1** to provide insight into the conformational transition pathway of the helix α4.

In the crystal structure of the *apo* human MGL [15], the protein crystallized in I222 space group as a dimer, with the two monomers per asymmetric unit. This structure represents an open form. Analysis of the interface interactions in this structure shows that the lid-domain is distant from the interface. In the crystal structure of the bound human MGL [14], the protein crystallized in $C222_1$ space group as a monomer. This structure represents a closed form. The solution of both open and closed forms of MGL supports the interfacial activation of MGL that allows the enzyme to exist in two main conformational states, an open and a closed forms [15]. Using large-scale MD simulations, Rengachari et al. [33] also observed the existence of the stable open and closed conformations of MGL in solution. Furthermore, detailed comparison between the *apo* and bound forms reveals that the lid-domain undergoes a substantial rearrgemnet upon ligand binding with other regions showing only very small differences [14]. The above data may indicate that MGL can exist in the open and closed forms and the conformational change of the lid region may be induced by ligand binding.

Previously, Rengachari et al. [33] solved the crystal structures of MGL from the bacterium *Basillus* sp. H257 in the *apo* form (PDB ID: 3RM3) and in complex with phenylmethylsulfonyl fluoride (PDB ID: 3RLI). Remarkably, the

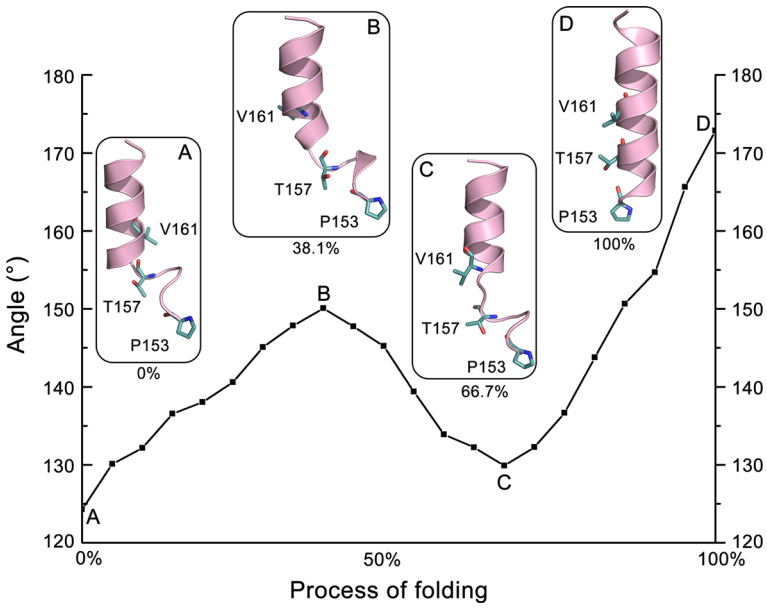

Fig. 6 The process for the conformational transition pathway of helix α4 obtained from the NEB simulations. (*A*) The initial state of helix α4 in the *apo* MGL. (*B*) The intermediate state represents a local maximum of the bending angle of helix α4. (*C*) The intermediate state represents a local minimum of the bending angle of helix α4. (*D*) The final state of the helix α4 in the compound **1**-bound MGL

cap structures (residues 119–164) of bacteria MGL corresponding to the lid-domain of human MGL adopt the open conformation in both structures of bacteria MGL. However, in both *apo* forms of bacteria and human MGLs, the cap region of bacteria MGL and the lid-domain of human MGL exhibit the same architecture despite very low sequence identity between them, indicating the structural conservation of the cap or lid-domain amongst MGL family [33].

The RMSD plots of the *apo* MGL and MGL-compound-**1** complex suggest that the two systems were stable during the 100 ns MD simulations. Lower RMSD values were obtained in the MGL-compound-**1** complex compared to the *apo* MGL indicates that the compound **1** plays a fundamental role in the stability of MGL. The calculation of RMSF has the ability to detect rigid and fluctuating residues in protein structure. It should be noted that the notable changes were observed in the lid-domain, while the other domains showed only very small differences. The higher RMSF values in the *apo* MGL accentuate the inherent flexibility of the lid-domain, which probably facilitates its displacement from the surface of the membrane during the ligand binding [14]. Analysis of the MD trajectories between the *apo* MGL and MGL-compound-**1** complex showed that the compound **1** induced the closed conformation of the active site of MGL and the complete folding of the helix α4.

Conventional all-atom MD simulations of biomacromolecules embedded in the explicit solvent have the potential to capture large conformational rearrangement to sample conformational ensembles at atomic level [34–37]. Of note, large-scale MD simulations are extraordinarily time-consuming [34]. Thus, NEB, a powerful algorithm that has been successful to explore large conformational changes in human glucokinase [38] and 23S rRNA [39], was used to investigate the conformational transition pathway of helix α4 induced by the compound **1**. Based on the results from NEB simulations, we revealed that in the overall process of folding (Supporting Information Video S1), an almost 180° counter-clockwise rotation of the helix α4 was observed in the compound **1**-bound state compared to the *apo* state, rendering the residues Pro153, Thr157, and Val161 point to the same direction. The resulting conformational transition of helix α4 induced by the compound **1** may change the electrostatic surface of helix α4, thereby leading to the MGL dissociation from the membrane upon completion of the catalytic cycle [14].

5 Conclusions

Here, conventional MD and NEB simulations were carried out to investigate the conformational transition pathway of the helix α4 in the inhibitor binding process of human MGL. Conventional MD simulations revealed that binding of compound **1** to the active site of MGL enabled to reduce the RMSF values of the lid-domain. Furthermore, founded on the distance analysis between the helices α4 and α6 and the DCCM analysis, the compound **1** induced the closed conformation of the active site of MGL and reduced the conformational flexibility of the helix α4. Specially, the analyses of DSSP of the helix α4 and the helical bending angle ($C_\alpha^{Pro153}\cdots C_\alpha^{Thr157}\cdots C_\alpha^{Val161}$) between the *apo* and compound **1**-bound MGL demonstrated that the compound **1** induced the large-scale conformational rearrangement of the helix α4, leading to the complete folding of the helix α4. Moreover, NEB simulations unveiled that the

conformational transition pathway of helix α4 from the uncoiling state of the N-terminal residues (residues 153–157) in the *apo* MGL to the complete folding of the helix α4 in the compound **1**-bound MGL underwent an almost 180° counter-clockwise rotation of the helix α4. These results will provide an opportunity to further optimize the interactions between the MGL and its non-covalent inhibitions to design more potent and selective MGL inhibitors.

Acknowledgments This study was supported by the National Key Basic Research Program of China (973 Program, No. 2011CBA00800), the Open Funding Project of National Key Laboratory of Biochemical Engineering, and the Key Agriculture Support Project of Jiangsu Province (No. BE2013400).

References

1. Matsuda LA, Lolait SJ, Brownstein MJ, Young AC, Bonner TI (1990) Structure of a cannabinoid receptor and functional expression of the cloned cDNA. Nature 346:561–564
2. Munro S, Thomas KL, Abu-Shaar M (1993) Molecular characterization of a peripheral receptor for cannabinoids. Nature 365:61–65
3. Karlsson M, Contreras JA, Hellman U, Tornqvist H, Holm C (1997) cDNA cloning, tissue distribution, and identification of the catalytic traid of monoglyceride. Evolutionary relationship to esterases, lysophospholipases, and haloperoxidases. J Biol Chem 272:27218–27223
4. Dinh TP, Carpenter D, Leslie FM, Freund TF, Katona I, Sensi SL, Kathuria S, Piomelli D (2002) Brain monoglyceride lipase participating in endocannabinoid inactivation. Proc Natl Acad Sci USA 99:10819–10824
5. Saario SM, Laitinen JT (2007) Monoglyceride lipase as an enzyme hydrolyzing 2-arachidonoylglycerol. Chem Biodivers 4:1903–1913
6. Chon SH, Zhou YX, Dixon JL, Storch J (2007) Intestinal monoacylglycerol metabolism: developmental and nutritional regulation of monoacylglycerol lipase and monoacylglycerol acyltransferase. J Biol Chem 282:33346–33357
7. Dinh TP, Freund TF, Piomelli D (2002) A role for monoglyceride lipase in 2-arachidonoylglycerol inactivation. Chem Phys Lipids 121:149–158
8. Gonsiorek W, Lunn C, Fan X, Narula S, Lundell D, Hipkin RW (2000) Endocannabinoid 2-arachidonyl glycerol is a full agonist through human type 2 cannabinoid receptor: antagonism by anandamide. Mol Pharmacol 57:1045–1050
9. Maresz K, Carrier EJ, Ponomarev ED, Hillard CJ, Dittel BN (2005) Modulation of the cannabinoid CB2 receptor in microglial cells in response to inflammatory stimuli. J Neurochem 95:437–445
10. Vandevoorde S, Jonsson KO, Labar G, Persson E, Lambert DM, Fowler CJ (2007) Lack of selectivity of URB602 for 2-oleoylglycerol compared to anandamide hydrolysis in vitro. Br J Pharmacol 150:186–191
11. Long JZ, Li W, Booker L, Burston JJ, Kinsey SG, Schlosburg JE, Pavón FJ, Serrano AM, Selley DE, Parsons LH, Lichtman AH, Cravatt BF (2009) Selective blockade of 2-arachidonoylglycerol hydrolysis produces cannabinoid behavioral effects. Nat Chem Biol 5:37–44
12. Saario SM, Salo OM, Nevalainen T, Poso A, Laitinen JT, Jarvinen T, Niemi R (2005) Characterization of the sulfhydryl-sensitive site in the enzyme responsible for hydrolysis of 2-arachidonoyl-glycerol in rat cerebellar membranes. Chem Biol 12:649–656
13. Bertrand T, Augé F, Houtmann J, Rak A, Vallée F, Mikol V, Berne PF, Michot N, Cheuret D, Hoornaert C, Mathieu M (2010) Structural basis for human monoglyceride lipase inhibition. J Biol Chem 396:663–673
14. Schalk-Hihi C, Schubert C, Alexander R, Bayoumy S, Clemente JC, Deckman I, DesJarlais RL, Dzordzorme KC, Flores CM, Grasberger B, Kranz JK, Lewandowski F, Liu L, Ma H, Maguire D, Macielag MJ, McDonnell ME, Haarlander TM, Miller R, Millgan C, Reynolds C, Kuo LC (2011) Crystal structure of a soluble form of human monoglyceride lipase in complex with an inhibitor at 1.35 Å resolution. Protein Sci 20:670–683
15. Labar G, Bauvois C, Borel F, Ferrer J-L, Wouters J, Lambert DM (2010) Crystal structure of the human monoacylglycerol lipase, a key actor in endocannabinoid signaling. ChemBioChem 11:218–227
16. Case DA, Darden TA, Cheatham TE III, Simmerling CL, Wang J, Duke RE, Luo R, Walker RC, Zhang W, Merz KM, Roberts BP, Wang B, Hayik S, Roitberg A, Seabra G, Kolossvary I, Wong KF, Paesani F, Vanicek J, Liu J, Wu X, Brozell SR, Steinbrecher T, Gohlke H, Cai Q, Ye X, Wang J, Hsieh MJ, Cui G, Roe DR, Mathews DH, Seetin MG, Sagui C, Babin V, Luchko T, Gusarov S, Kovalenko A, Kollman PA (2010) AMBER 11. University of California, San Francisco
17. Frisch MJ, Trucks GW, Schlegel HB, Scuseria GE, Robb MA, Cheeseman JR, Scalmani G, Barone V, Meuuucci B, Petersson GA, Nakatsuji H, Caricato M, Li X, Hratchian HP, Izmaylov AF, Bloino J, Zheng G, Sonnenberg JL, Hada M, Ehara M, Toyota K, Fukuda R, Hasegawa J, Ishida M, Nakajima T, Honda Y, Kitao O, Nakai H, Vreven T, Montgomery JA, Peralta Jr. JE, Ogliaro F, Bearpark M, Heyd JJ, Brothers JJHE, Kudin KN, Staroverov VN, Kobayashi R, Normand J, Raghavachari K, Rendell A, Burant JC, Iyengar SS, Tomasi J, Cossi M, Rega N, Millam JM, Klene M, Knox JE, Cross JB, Bakken V, Adamo C, Jaramillo J, Gomperts R, Stratmann RE, Yazyev O, Austin AJ, Cammi R, Pomelli C, Ochterski JW, Martin RL, Morokuma K, Zakrzewski VG, Voth GA, Salvador P, Dannenberg JJ, Dapprich S, Daniels AD, Farkas O, Foresman JB, Ortiz JV, Cioslowski J, Fox DJ (2009) Gaussian 09. Gaussian Inc., Wallingford
18. Duan Y, Wu C, Chowdhury S, Lee MC, Xiong G, Zhang W, Yang R, Cieplak P, Luo R, Lee T (2003) A point-charge force field for molecular mechanics simulations of proteins. J Comput Chem 24:1999–2012
19. Jorgensen WL, Chandrasekhar J, Madura JD, Impey RW, Klein ML (1983) Comparison of single potential function for simulating liquid water. J Chem Phys 79:926–935
20. Lu S-Y, Huang Z-M, Huang W-K, Liu X-Y, Chen Y–Y, Shi T, Zhang J (2013) How calcium inhibits the magnesium-dependent kinase GSK3β: a molecular simulation study. Proteins 81:740–753
21. Lu S, Huang W, Li X, Huang Z, Liu X, Chen Y, Shi T, Zhang J (2012) Insights into the role of magnesium in *myo*-inositol monophosphatase: metal mechanism, substrate binding, and lithium therapy. J Chem Inf Model 52:2398–2409
22. Lu S-Y, Jiang Y-J, Zou J-W, Wu T-X (2011) Molecular modeling and molecular dynamics studies of the GSK3β/ATP/substrate complex: understanding the unique P + 4 primed phosphorylation specificity for GSK3β substrates. J Chem Inf Model 51:1025–1036
23. Darden T, York D, Pedersen L (1993) Particle mesh Ewald: an N log(N) method for Ewald sums in large systems. J Chem Phys 98:10089–10092
24. Ryckaert JP, Ciccotti G, Berendsen HJC (1977) Numerical integration of the cartesian equations of motion of a system with constraints: molecular dynamics of n-alkanes. J Comput Phys 23:327–341

25. Wu X, Brooks BR (2003) Self-guided Langevin dynamics simulation method. Chem Phys Lett 381:512–518
26. Papaleo E, Lindorff-Larsen K, De Gioia L (2012) Paths of long-range communication in the E2 enzymes of family 3: a molecular dynamics investigation. Phys Chem Chem Phys 14:12515–12525
27. Henkelman G, Jónsson H (2000) Improved tangent estimate in the nudged elastic band method for finding minimum energy paths and saddle points. J Chem Phys 113:9978–9985
28. Bergonzo C, Campbell AJ, Walker RC, Simmerling C (2009) A partial nudged elastic band implementation for use with large or explicitly solvated systems. Int J Quant Chem 109:3781–3790
29. Kabsch W, Sander C (1983) Dictionary of protein secondary structure: pattern recognition of hydrogen-bonded and geometrical features. Biopolymers 22:2577–2637
30. Jalkute CB, Barage SH, Dhanavade MJ, Sonawane KD (2013) Molecular dynamics simulation and molecular docking studies of angiotensin concerting enzyme with inhibitor lisinopril and amyloid beta peptide. Protein J 32:356–364
31. Ezat AA, EI-Bialy NS, Mostafa HIA, Ibrahim MA (2014) Molecular docking investigation of the binding interactions of macrocyclic inhibitors with HCV NS3 protease and its mutants (R155K, D168A and A156V). Protein J 33:32–47
32. Lu S-Y, Jiang Y-J, Zou J-W, Wu T-X (2012) Effect of double mutations K214/A-E215/Q of FRATide on GSK3β: insights from molecular dynamics simulation and normal mode analysis. Amino Acids 43:267–277
33. Rengachari S, Bezerra GA, Riegler-Berket L, Gruber CC, Sturm C, Tashler U, Boeszoermenyi A, Dreveny I, Zimmermann R, Gruber K, Oberer M (2012) The structure of monoacylglycerol lipase from *Bacillus* sp. H257 reveals unexpected conservation of the cap architecture between baterial and human enzymes. Biochim Biophys Acta 1821:1012–1021
34. Saladino G, Gervasio FL (2012) New insights in protein kinase conformational dynamics. Curr Top Med Chem 12:1889–1895
35. Md S, Rauf A, Endou A, Takaba H, Miyamoto A (2013) Effect of Y220C mutation on p53 and its rescue mechanism: a computer chemistry approach. Protein J 32:68–74
36. Srikumar PS, Rohini K, Rajesh PK (2014) Molecular dynamics simulations and principal component analysis on human laforin mutation W32G and W32G/K87A. Protein J 33:289–295
37. Lu S, Jiang Y, Lv J, Zou J, Wu T (2011) Mechanism of kinase inactivation and nonbinding of FRATide to GSK3β due to K85M mutation: molecular dynamics simulation and normal mode analysis. Biopolymers 95:669–681
38. Huang M, Lu S, Shi T, Zhao Y, Chen Y, Li X, Liu X, Huang Z, Zhang J (2013) Conformational transitional pathway in the activation process of allosteric glucokinase. PLoS ONE 8:e55857
39. Réblová K, Střelcová Z, Kulhánek P, Beššeová I, Mathews DH, Nostrand KV, Yildirim I, Turner DH, Sponer J (2010) An RNA molecular switch: intrinsic flexibility of 23S rRNA helices 40 and 68 5'-UAA/5'-GAN internal loops studied by molecular dynamics methods. J Chem Theory Comput 6:910–929